RSC Advances

ROYAL SOCIETY OF CHEMISTRY

www.rsc.org/advances

Improved carrier mobility and bandgap tuning of zinc doped bismuth oxide

M. J. Jabeen Fatima, A. Navaneeth, S. Sindhu*

Zinc doped bismuth oxides shows tuned bandgap and electronic properties with an improved charge carrier mobility and conductivity.

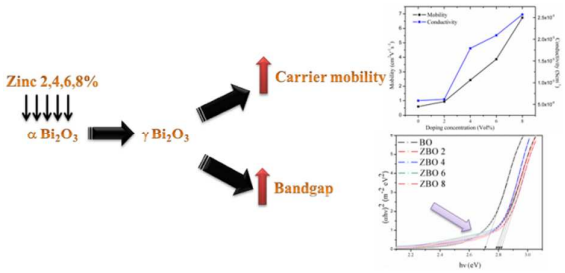

Cite this: DOI: 10.1039/c0xx00000x

www.rsc.org/xxxxxx

ARTICLE TYPE

Improved carrier mobility and bandgap tuning of zinc doped bismuth oxide

M. J. Jabeen Fatima, A. Navaneeth, S. Sindhu*

Received (in XXX, XXX) Xth XXXXXXXXX 20XX, Accepted Xth XXXXXXXXX 20XX

DOI: 10.1039/b000000x

The present work attempts to synthesize bismuth oxide and zinc doped bismuth oxide by citrate gel method to tune the electronic and optical properties suitable for different opto-electronic applications. Techniques like ICP-AES and EDAX were used to determine the compositions of metal in the doped samples. Thermal analyses such as TGA-DTA were used to study the phase change and decomposition temperature of the samples to fix the sintering temperature. Later, the phase purity and crystallinity of sintered and unsintered metal oxides were determined from powder X-ray analysis. The morphology and average particle sizes were obtained from SEM imaging. The doped bismuth oxide shows an increase in bandgap with increase in zinc percentage, which is estimated from DRS measurements. Bulk carrier concentration, sheet concentration, resistivity, conductivity and charge carrier mobility of doped and undoped samples were obtained from hall measurements and the data showed improvement in conductivity and carrier mobility on doping. Increase in carrier mobility and conductivity is attributed to relatively less grain barriers due to the smaller size of the doped samples.

1. Introduction

Bismuth oxide is being extensively studied by the researchers nowadays due to its wide range of applications in various fields. The important applications of bismuth oxide include photocatalysis[1-3], photovoltaics[4], supercapacitors[5], sensors [6,7]etc. Bismuth oxide exists in four major polymorphic forms such as α, β, γ, and δ with crystal structures respectively monoclinic, tetragonal, bcc, and fcc. The α form is naturally stable at ambient condition and at elevated temperatures it gets converted to δ form. All other forms are metastable states stabilized at different conditions. The stability of the polymorphs depends on the method of synthesis adopted. Many reports are found on the stabilized metastable forms of bismuth oxide[8]. The δ form is known to be the most conducting polymorph of bismuth oxide[9,10]. The increased ionic conductivity arises due to the increased oxygen ion vacancies[11].

Reports show that methods like sol-gel and hydrothermal were widely used for the synthesis of bismuth oxide[12,13]. Sol-gel is the commonly adopted synthetic approach due to its easiness in achieving phase pure metal oxides in large quantity. In sol-gel method we have adopted citrate gel method, as citrate is a nontoxic organic material cheaply available.

Bismuth oxide is a wide bandgap semiconductor with bandgap varying in the range 2.0 to 3.96 eV[12] and the bulk bandgap reported is 2.75eV. Parameters like bandgap and conductivity are of utmost importance while considering these materials for optoelectronic applications. Both these parameters can be tuned easily by polymorph selective synthesis of bismuth oxide[14]. Doping has a major role in polymorph selective synthesis by stabilizing the metastable phase of bismuth oxide. The metastable phase has better conductivity than the normal stable phase[15, 16].

The γ phase of bismuth oxide was prepared earlier by precipitation method[16]. Here, we report the synthesis of α bismuth oxide and stabilization of γ bismuth oxide on doping the samples with different volume percentage of zinc. A detailed study is carried out on the syntheses, optical and electronic properties of pure and zinc doped bismuth oxide systems. An attempt was made to improve the properties such as bandgap, carrier concentration, conductivity and mobility of the doped metal oxide.

2. Experimental

Synthesis of metal oxides

Bismuth oxide was synthesized by the well known citrate gel method but with slight modifications[17]. The precursor, bismuth nitrate pentahydrate, ($BiNO_3$ $5H_2O$, 0.16M, 2.328g) was dissolved in nitric acid, (HNO_3) followed by dilution in a ratio of 1:3. The mixture was heated in a water bath maintained at 373K. To this hot mixture, equimolar citric acid, ($C_6H_8O_7$, 0.16M, 0.9222g) was added and maintained in the same condition until pale yellow gel formed. The gel was then heated using a heating mantle, and converted to foam which combusted itself to form the final product. Products thus obtained were sintered at 700°C for 120 minutes in a muffle furnace to obtain phase pure metal oxides.

Zinc doped bismuth oxide was also synthesized by the same method. The precursor, zinc nitrate hexahydrate, ($Zn(NO_3)_26H_2O$, 0.16M) was mixed with bismuth nitrate pentahydrate before dissolving in nitric acid. Zn doping in different percentage (2, 4,

6, and 8 volume percentage) was done by maintaining the volume constant. The samples were named BO for bismuth oxide and ZBO 2, ZBO 4, ZBO 6, and ZBO 8 for Zn doped by volume percentages of 2, 4, 6, and 8 respectively. The samples before sintering were mentioned with a suffix 'US'.

Characterization

The synthesized metal oxides were characterized by various characterization techniques. The phase transition temperature and the decomposition temperature were analyzed by using thermogravimetric and differential thermal analysis (TGA-DTA) using Pelkin Elmer STA 6000 above 800°C and then the sintering temperature was fixed. The phase purity and crystallinity of metal oxide before and after sintering were obtained from X-ray Diffraction analysis (XRD) by using Rigaku miniplex X-Ray diffractometer (Cu Kα - 0.15496nm), scanned between 20-80°. The composition of the metal was determined from Inductively Coupled Plasma Atomic Emission Spectrum (ICP-AES) from Thermo Electron IRIS INTREPID II XSP DUO. The presence of dopant was confirmed from Energy Dispersive Spectrum (EDS) measurements by using JEOL Model JED-2300. The morphology and size of the synthesized metal oxides were obtained by using Scanning Electron Microscopy (SEM) images from JEOL Model JSM 6390LV. The bandgap of the samples were determined from Tauc plot drawn using the diffuse reflectance spectrum (DRS) obtained from JASCO UV-Visible spectrophotometer in the wavelength range 200 to 600 nm. The photoluminescence measurements were done by using Fluoromax 4P of Horiba. The Hall measurements were carried out to obtain the carrier mobility, resistivity, conductivity, bulk concentration and sheet concentration using Ecopia HMS 5300. The samples were coated on a glass plate in an area of $1cm^2$ and contact was given using indium metal at four edges.

3. Results and Discussions

Thermogravimetric analyses of unsintered samples were carried out to study the thermal behaviour of the samples. The TGA-DTA graph of BO is given in figure.1. Three major thermal changes are observed from the figure, where the first change is observed around 100°C, which is attributed to the evaporation of excess water from the samples. The second endotherm at around 400°C is assumed to be due to the decomposition of the excess carbonaceous materials remaining in the samples. The third change is found at 730°C due to the phase change of bismuth oxide. At 730°C, the α phase of bismuth oxide is converted to the δ phase and finally the samples are decomposed around 870°C. The parameters related to the thermal changes of doped and undoped metal oxides are given in table 1. All the samples showed similar behaviour with very slight changes in temperatures. The sintering temperature was fixed at 700°C based on the observed phase change at 730°C in TGA-DTA. The TGA-DTA graphs of all the doped samples are given in the supporting information (Figures S1-S4).

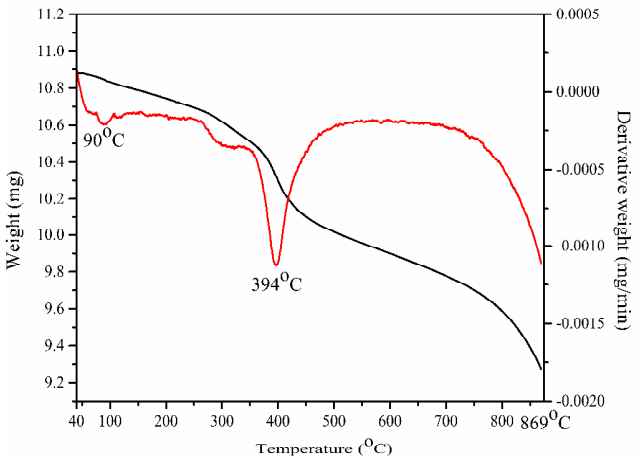

Fig.1. TGA-DTA spectrum of bismuth oxide

Table 1 Second endotherm and decomposition temperature of bismuth oxide and zinc doped bismuth oxide

Samples	Second endotherm °C	Decomposition temperature °C
BO	394	869
ZBO 2	390	869
ZBO 4	393	869
ZBO 6	410	869
ZBO 8	414	869

The structural and phase identification of the prepared samples were done by using X-ray diffraction (XRD) analysis. The XRD patterns of pure bismuth oxide at sintered (BO) and unsintered (BO US) conditions are shown in figure 2. These XRD patterns are compared with the standard JCPDS file number 76-1730 which corresponds to the monoclinic phase with space group $P2_1/c$ (14) of bismuth oxide and the extra peaks observed for the unsintered bismuth oxide indicate the presence of impurities. However, the pure phase is obtained after sintering the samples at 700°C.

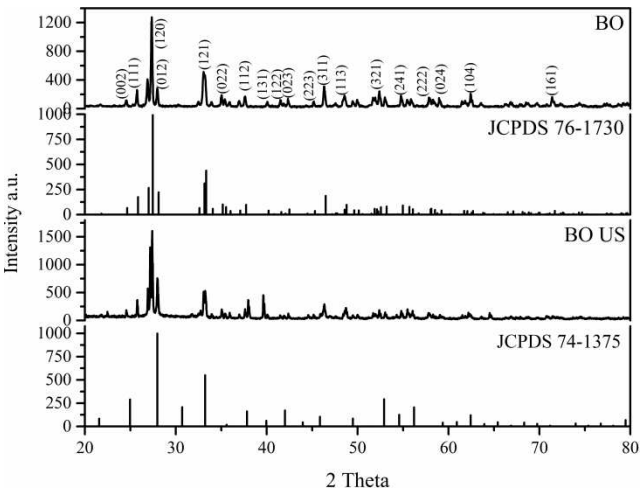

Fig.2. XRD of bismuth oxide before and after sintering compared with the standard JCPDS file No 76-1730

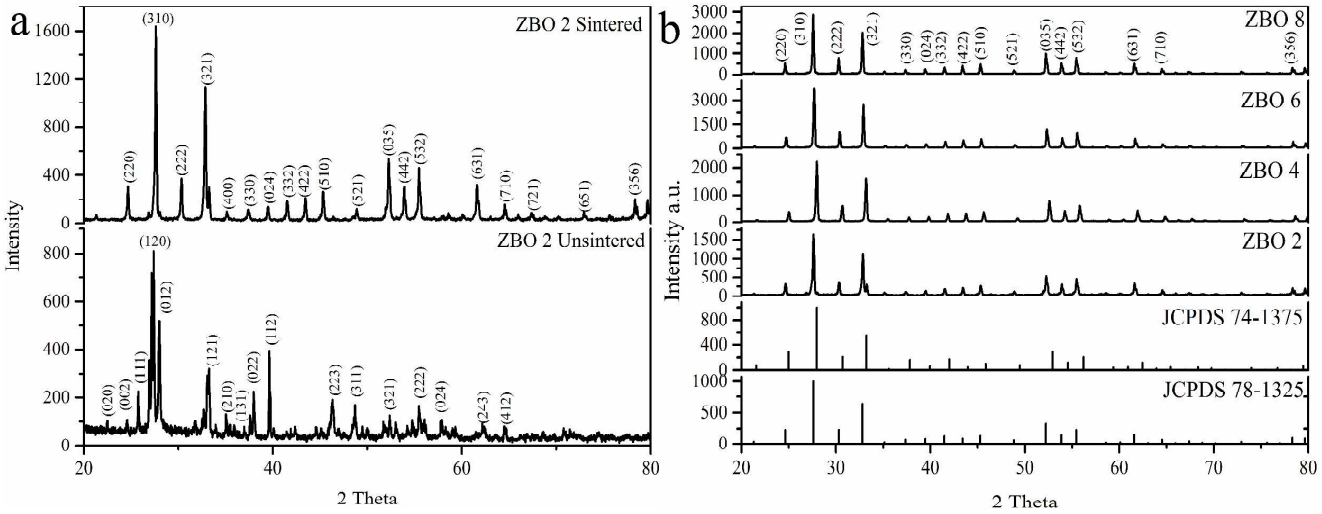

Fig.3. X-Ray diffraction pattern (a) ZBO 2 samples before and after sintering (b) ZBO 2,4,6, and 8 samples compared with the standard JCPDS files 74-1375 and 78-1325

The X-Ray diffraction analysis of doped samples before and after sintering shows different behaviour (Figure 3a). The samples before sintering shows similar XRD pattern of α phase bismuth oxide and a difference in peak positions after sintering. The doped samples correspond to the body centred cubic phase of bismuth oxide (γ phase – JCPDS file no 74-1375)[12], where the pattern (Figure 3b) is very similar to bismuth zinc oxide (JCPDS file no 78-1325, $Bi_{12}ZnO_{20}$). The stabilized γ phase of bismuth oxide was reported earlier at room temperature[16]. From the XRD data it can be concluded that the zinc has entered the lattice of bismuth ions as a result of doping.

The XRD pattern of unsintered ZBO 2 sample shows (Figure 3a) a weak peak due to [121] plane of the α phase bismuth oxide, indicating incomplete conversion of γ phase even after sintering at 700°C. But rest of the doped samples didn't show any peaks due to α phase leading to the inference that at lower percentage of doping, the zinc atoms are insufficient for the complete conversion of γ phase.

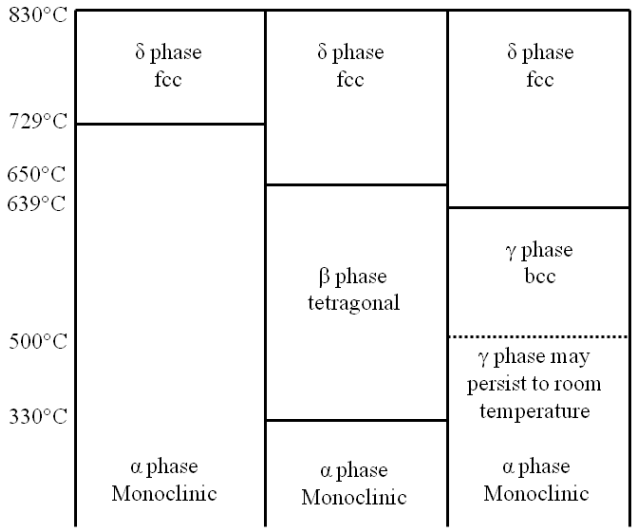

Fig.4. Phase change of bismuth oxide on cooling[15]

A chart showing the temperature dependent phase change of bismuth oxide is given in figure 4. On heating, the α phase is converted to δ phase at 730°C and that phase change is observed in the TGA-DTA curve of the samples with an indication of weight change at around 730°C. The metal oxide formed metastable phases, such as tetragonal β and bcc γ phases on cooling at different conditions. Usually, on further cooling, these phases get transformed to the most stable α phase. But under certain conditions like doping, the metastable forms stabilize. In the current work, the γ phase is stabilized on cooling when zinc is added as a dopant. The XRD of doped samples confirms the effect of doping in stabilizing the metastable phase. The crystallite sizes of the samples are calculated from XRD using Scherrer's formula and it shows a decrease in crystallite size with zinc doping. The calculated size for bismuth oxide (BO) is ~57 nm and in the case of doped samples it varies from 55 to 45 nm, when doping percentage changes from 2 to 8 vol%. The table showing FWHM and crystallite size is given in supporting information (Table S1).

Raman spectra of the samples were recorded (Figure 5) and in the case of BO it confirms the α phase of bismuth oxide. With an increase in Zn doping concentration from 2 to 8 volume percentages, the peaks around 93, 150, 185, 211, and 450 cm^{-1} are found to diminish and finally vanish. The vanished peaks correspond to the characteristic peaks of α phase of bismuth oxide[18]. Certain additional peaks at 258, 377, 531, and 625 cm^{-1} are found to appear on increasing the doping concentration. These peaks are the characteristic peaks corresponding to the γ phase of bismuth oxide[19]. Hence both XRD and Raman spectra substantiate the fact that at lower doping concentration both α and γ phases exist and further increase in doping concentration stabilizes the metastable γ phase. Individual Raman spectra of the samples are given in the supporting information (Figures S5 to S9).

The results obtained from ICP-AES corroborate the percentage of the metals in the doped metal oxides. The value calculated from the amount of precursor taken is given as theoretical value

which is compared with the values obtained from the analyses with an error percentage of ±0.2. Details are listed in Table.2. The presence of the metal is also confirmed from the EDS measurement obtained with SEM analysis and the details are given in supporting information (Figure S10).

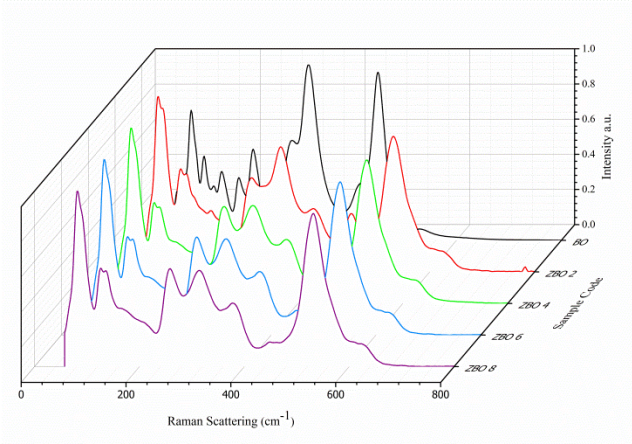

Fig.5 Raman spectra of BO, ZBO 2, 4, 6, and 8

Table 2 ICP-AES values compared with theoretical values

Sample code	Zn (%)		Bi (%)	
	Theoretical	ICP-AES	Theoretical	ICP-AES
BO	0	0	100	100
ZBO 2	0.635	0.69	99.37	99.31
ZBO 4	1.29	1.529	98.71	98.47
ZBO 6	1.96	2.00	98.04	98.00
ZBO 8	2.65	2.73	97.35	97.26

The morphology of the samples is analyzed by SEM and the images of BO, ZBO 2, and ZBO 8 are shown in figure 6. The SEM images show hazy morphology with variable particle size and hence size determination is found to be difficult from the images obtained.

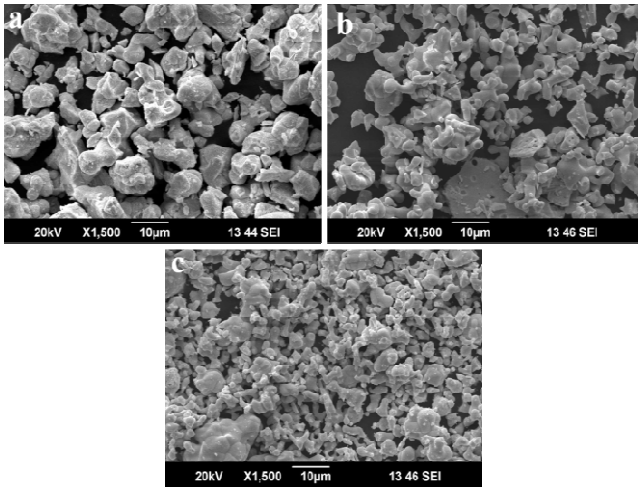

Fig.6 SEM image of (a) BO (b) ZBO 2 (c) ZBO 8

Figure 7a depicts the Diffuse Reflectance Spectra (DRS) of both doped and undoped samples of bismuth oxide. From the DRS it is clear that both the doped and undoped samples absorb in the UV-Visible region. The bandgap of the samples are determined from Tauc plot by plotting $(\alpha h\nu)^{1/2}$ Vs hν (Figure 7b). The tangent of the plot extrapolated to the X axis gives the bandgap of the semiconductor. For pure bismuth oxide, the extrapolation coincides X axis at 2.7 eV which corresponds to the bandgap of bulk bismuth oxide. Similar methods are adopted to determine the bandgap of zinc doped bismuth oxide samples. The bandgap is also determined from the PL measurements. On plotting PL intensity Vs hν, the peak maxima indicate the bandgap of the samples[20]. The graph is given in the supporting information (Figure S11). The values obtained from both the methods are compared and tabulated (Table 3). The values are almost the same in both the cases. A slight increase in bandgap is observed due to the effect of increase in dopant concentration for the doped samples.

Table 3 Bandgap of pure and Zn doped bismuth oxide calculated from Tauc plot and PL spectrum

Samples	Bandgap from Tauc's plot	Bandgap from PL Spectrum
BO	2.70 eV	2.71 eV
ZBO 2	2.78 eV	2.78 eV
ZBO 4	2.79 eV	2.79 eV
ZBO 6	2.80 eV	2.80 eV
ZBO 8	2.81 eV	2.81 eV

The emission spectra of the samples are recorded by exciting at the band edge of absorption and the graphs are shown in figure 8. Table 4 lists the photoluminescence parameters, such as the excitation and emission wavelength of pure and Zn doped bismuth oxides. The excitation wavelength of pure bismuth oxide is 416 nm and in the case of doped samples it is taken as 403 nm based on the DRS spectra recorded for these samples. From figure 8 it is clear that the major emission peak of pure bismuth oxide is at 466 nm and this is due to the band edge from the recombination of free excitons. Here, the photons are emitted as a result of the de-excitation of electron from the p level to the s level of bismuth ion[16].

Table 4 Photoluminescence parameters of pure and Zn doped samples

Sample code	Excitation wavelength nm	Emission Wavelength nm
BO	416	456
ZBO 2	403	440
ZBO 4	403	443
ZBO 6	403	442
ZBO 8	403	439

Zinc doping shows marked changes in the PL spectrum with the appearance of major emission peak at 441 nm due to the band edge emission of the free exciton recombination. The other peaks in the Zn doped samples at 470, 495, and at 549 nm are due to the introduction of defect states. The peak at 470 nm arises from the recombination between the Zn vacancies or Zn interstitial to the valence band[21,22]. The other peak at 495 nm is ascribed to the deep level emission resulting from surface defects[23].

The peak at 549 nm is attributed to the defect emission due to oxygen ion vacancies, or oxygen interstitials in the system. It has even been attributed to Zn vacancy in the case of ZnO nanoparticles[24,25]. Usually this peak appears intense and broad due to the chemisorptions of oxygen. However, in this study the intensity is comparatively low indicating the moderate percentage

of defects in the samples.

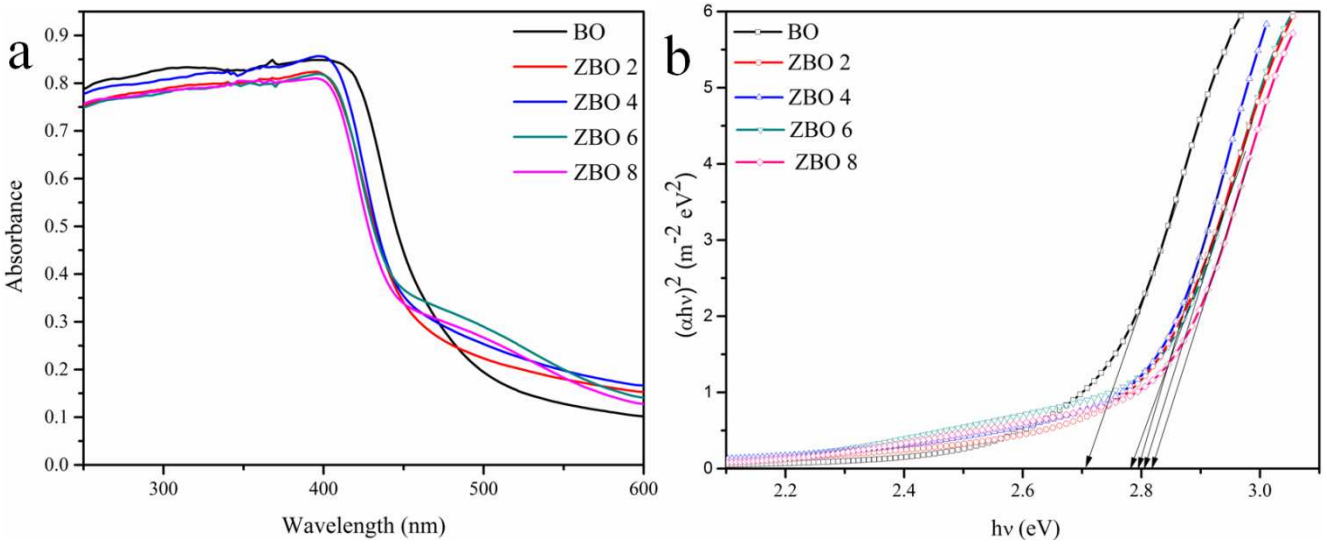

Fig.7 Diffuse reflectance spectrum of (a) BO and ZBO 2, 4, 6, and 8 (b) Tauc's plot of pure and doped bismuth oxide

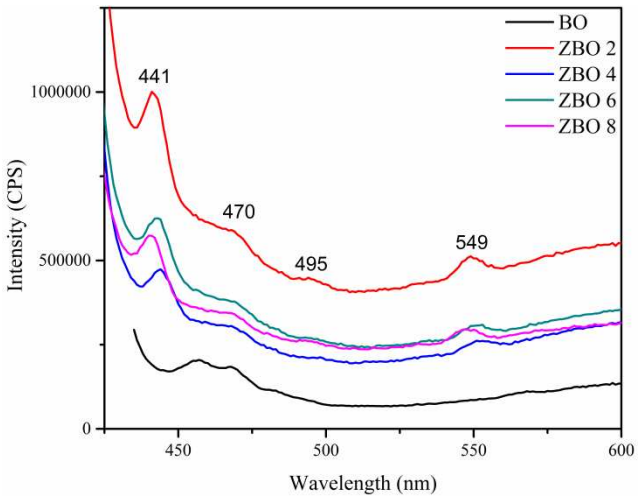

Fig.8 Photoluminescence spectra of pure and Zn doped bismuth oxide

Hall measurements of the samples have been carried out by the commonly adopted Van der Pauw method to study the effect of doping in the conductivity, carrier concentration and mobility of the samples. The samples show n- type doping with a linear increase in carrier mobility and conductivity with increasing doping concentration[26] (Figure 9). Maximum conductivity of $2.57x10^{-5}$ S/cm is obtained for ZBO 8 with an improved mobility of 6.74 cm^2/V.s. The reason for improved charge carrier mobility in the samples on doping is the decrease in scattering probability of the carrier[27]. The size of zinc ions is lower than that of bismuth ions (ionic radius of Bi^{3+} is 1.17Å[28] and that of Zn^{2+} is 0.74Å[29]) and hence there is less scattering of the electron leading to an enhancement in the carrier mobility as doping percentage increases. In addition to that, the crystallite size calculated from XRD indicates a decrease in size with Zn doping, which further correlates the mobility of the carrier with minimized grain barrier. The details of carrier type, resistivity, conductivity and mobility of the measured samples are given in table 5.

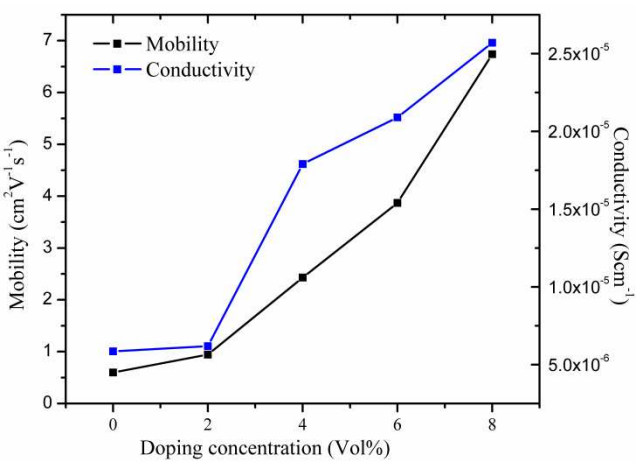

Fig.9 Conductivity and mobility variation with Zn doping in bismuth oxide

Table 5 Hall measurement analysis of pure and zinc doped bismuth oxide

Sample code	Carrier Concentration cm^{-3}	Carrier type	Resistivity Ωcm	Conductivity Scm^{-1}	Mobility cm^2/V.s
BO	$-6.12x10^{13}$	n	$1.71 x10^5$	$5.85 x10^{-6}$	0.597
ZBO 2	$-4.10 x10^{13}$	n	$1.62 x10^5$	$6.19 x10^{-6}$	0.943
ZBO 4	$-4.61 x10^{13}$	n	$5.58 x10^4$	$1.79 x10^{-5}$	2.43
ZBO 6	$-3.37 x10^{13}$	n	$4.79 x10^4$	$2.09 x10^{-5}$	3.87
ZBO 8	$-2.38 x10^{13}$	n	$3.89 x10^4$	$2.57 x10^{-5}$	6.74

Conclusions

Bismuth oxide, and doped bismuth oxide with different volume percentage of zinc are prepared by citrate gel method. XRD and Raman analyses of the prepared samples show that pure bismuth oxide forms stable α phase but the doped samples stabilizes the metastable γ phase of bismuth oxide. Optical studies by DRS and PL reveal that the Zn doped bismuth oxide shows an increase in bandgap with increase in zinc concentration. Doping improved the carrier mobility and the conductivity of the samples which is

attributed to relatively less grain barriers due to the smaller size of the doped samples. More detailed studies on the use of these materials for photovoltaic application are in progress.

Acknowledgements

M J. Jabeen Fatima would like to acknowledge Council for Scientific and Industrial Research (CSIR), Government of India, for the Junior Research Fellowship (JRF). S. Sindhu acknowledges KSCSTE, Government of Kerala and CSIR, Government of India for the financial support received in the form of research projects. The analyses were carried out at Sophisticated Analytical and Instrumentation Facility (SAIF) available at Indian Institute of Technology (IIT) Bombay, IIT Madras and Cochin University of Science & Technology (CUSAT). Morphological and Hall measurements were carried out respectively at National Institute of Technology (NIT) Calicut and NIT Trichy.

Notes

Department of Nanoscience and Technology, University of Calicut, Thenhipalam- 673635, Kerala, India;
Fax: 91 494 2400269; Tel: 91 494 2407373;
**E-mail: sindhu.swaminath@gmail.com*

† Electronic Supplementary Information (ESI) available: The graphs of TGA-DTA, images of EDX ,PL and Raman graph attached.

References

1 Yu-Chun Wu, Yu-Chen Chaing, Chi-Yuen Huang, Sea-Fue Wang, Hue-Yu Yang, *Dyes Pigments*, 2013, **98,** 25.
2 Subramanian Balachandran, Meenakshisundaram Swaminathan, *J. Phys. Chem.C*., 2012, **116**, 26306.
3 Manickavachagam Muruganandham, Ramakrishnan Amutha, Gang-Juan Lee, Shu-Han Hsieh, Jerry J Wu, Mika Sillanpaa, *J. Phys. Chem.C.*, 2012,**116,** 12906.
4 Waleed E Mahmoud, A A Al-Ghamdi, *Polym. Advan. Technol.*, 2009, **22**, 877.
5 Fu-Lin Zheng, Gao-Ren Li, Yan- Nan Ou, Zi-Long Wang, Cheng-Yong Su, Ye-Xiang Tong, *Chem. Commun*., 2010, **46**, 5021.
6 A. Cabot, A. Marsal, J. Aribol, J. R. Morante, *Sensor actuat B-Chem*, 2004, **99**, 74.
7 Sambhaji S. Bhande , Rajaram S. Mane, Anil V. Ghule, Sung-Hwan Han, *Scripta Mater***,** 2011, **65**, 1081.
8 O.Monnereau, L. Tortet, P. Llewellyn, F. Rouquerol, G. Vacquier, *Solid State Ionics*, 2003, **157**, 163.
9 Chris D. Ling, Siegbert Schmid, Peter E. R. Blanchard, Vaclav Petříček, Garry J. McIntyre, Neeraj Sharma, Andrey Maljuk, Aleksey A. Yaremchenko, Vladislav V. Kharton, Matthias Gutmann, and Ray L. Withers, *J. Am. Chem. Soc.*, 2013, **135**, 6477.
10 Celia L. Gomez, Osmary Depablos-Rivera, Juan C. Medina, Phaedra Silva-Bermudez, Stephen Muhl, Andreas Zeinert, Sandra E. Rodil, *Solid State Ionics*, 2014, **255**, 147.
11 Guohua Zhong, Yao Wang, Zhenxiang Dai, Jianglong Wang, Zhi Zheng, *Phys. Status Solidi B*, 2009, **246**, 97.
12 He Weidong, Qin Wei, Wu Xiaohong, Ning Hailong, *Mater. Lett.*, 2007, **61**, 4100.
13 Hongbing Lu, Shimin Wang, Li Zhao, Bing Dong, Zuxun Xu, Jinchai Li, *RSC Adv*.,2012, **2**, 3374.
14 Yongfu Qiu, Minlin Yang, Hongbo Fan, Yuanzhi Zuo, Youyuan Shao, Yongjun Xu, Xiaoxi Yang, Shihe Yang, *Cryst Engg Comm*., 2011, **13**, 1843.
15 P. Shuk, H. –D. Wiemhöfer, U. Göpel, M Greenblatt, *Solid State Ionics*, 1996, **89**, 179.
16 Teng-Kuan Tseng, Jihun Choi, Doh-Won. Jung, Mark Davidson, Paul H Holloway, *ACS Appl Mater Inter*, 2010, **2**, 943.
17 M. Anilkumar, Renu Pasricha, V. Ravi, *Ceram. Int.* 2005, **31**, 889.
18 S. Venugopalan, A. K. Ramdas, *Phys. Rev. B*, 1972, **5**, 4065.
19 S. N. Narang, N. D. Patel, V. B. Kartha, *J. Mol. Struc.*, 1994, **324**, 221.
20 J. W. Lee, N. G. Subramaniam, J. C. Lee, S. Kumar. S, T. W. Kang, *EPL-Europhys Lett*, 2011, **95**, 47002.
21 R. Amiruddin, M. C. Santhosh Kumar, *Ceram. Intl.*, 2014, **40**, 11283.
22 H.A. Ahn, Y. Y. Kim, D. C. Kim, S. K. Mohanta, H. K. Cho, *J. Appl. Phys.*, 2009, **105**, 013502.
23 Bixia. Lin, Zhuxi. Fu, Yunbo. Jia, *Appl. Phys. Lett.*, 2001, **79**, 943.
24 Meghana. Ramani, S. Ponnusamy, C. Muthamizhchelvan, *Opt. Mater*, 2012, **34**, 817.
25 Q.X. Zhao, P. Kalson, M. WillanderH. M. Zhong, W. Lu, J.H. Yang, *Appl. Phys. Lett.*, 2005, **87**, 211912.
26 A. A. Dakhel, *Bull. Mater. Sci.,* 2013, **36**, 819.
27 E. Hendry, M. Koeberg, J. Pijpers, M. Bonn, *Phys. Rev. B*, 2007, **75**, 233202.
28 M. Prekajski, Z. Dohčević-Mitrović, M. Radović, B. Babić, J. Pantić, A. Kremenović, B. Mantović, *J. Eur. Ceram. Soc.*, 2012, **32**, 1983.
29 Jin-Hong. Lee, Byung-Ok Park, *Thin Solid Films*, 2003, **426**, 94.

